Extraordinary Performance of Carbon-Coated Anatase TiO_2 as Sodium-Ion Anode

Muhammad Nawaz Tahir, Bernd Oschmann, Daniel Buchholz, Xinwei Dou, Ingo Lieberwirth, Martin Panthöfer, Wolfgang Tremel, Rudolf Zentel, and Stefano Passerini**

The synthesis of in situ polymer-functionalized anatase TiO_2 particles using an anchoring block copolymer with hydroxamate as coordinating species is reported, which yields nanoparticles (≈11 nm) in multigram scale. Thermal annealing converts the polymer brushes into a uniform and homogeneous carbon coating as proven by high resolution transmission electron microscopy and Raman spectroscopy. The strong impact of particle size as well as carbon coating on the electrochemical performance of anatase TiO_2 is demonstrated. Downsizing the particles leads to higher reversible uptake/release of sodium cations per formula unit TiO_2 (e.g., 0.72 eq. Na^+ (11 nm) vs only 0.56 eq. Na^+ (40 nm)) while the carbon coating improves rate performance. The combination of small particle size and homogeneous carbon coating allows for the excellent electrochemical performance of anatase TiO_2 at high (134 mAh g^{-1} at 10 C (3.35 A g^{-1})) and low (≈227 mAh g^{-1} at 0.1 C) current rates, high cycling stability (full capacity retention between 2nd and 300th cycle at 1 C) and improved coulombic efficiency (≈99.8%).

1. Introduction

Lithium-ion batteries (LIBs) are considered to be the most promising battery technology for the combination with renewable energy sources and for future large scale and high-energy applications such as electric vehicles.[1] However, driven by the concern over the limited availability of lithium and other state-of-art-materials in LIBs,[2,3] the development of postlithium battery technologies has attracted more and more researchers. In this regard, the sodium-ion battery (SIB) technology takes the privilege over other promising stationary energy storage devices, including LIBs, for cost effective energy storage technology based on naturally abundant materials, which is a key parameter for stationary energy storage. In order to enable Na-based energy storage suitable electrode materials are being developed, capable of accommodating the larger Na-ions and enabling highly reversible (de-)sodiation as well as stable long-term cycling.

With respect to the negative electrode, materials undergoing conversion-alloying type reactions are rather challenging as they suffer of very large volume changes upon cycling due to the large Na^+-cation size,[4] but encouraging results, e.g., for $FeSe_2$ have been published recently by Zhang et al.[5] Instead, alloying based materials such as Sn[6–8] and Sb[9–11] as well as insertion/intercalation based materials such as hard carbon,[12–14] recently graphite[15] and titania and titanates like $Na_2Ti_3O_7$[16,17] and TiO_2[18] appear to be very promising anode materials. Different polymorphs of TiO_2 like TiO_2(B),[19,20] amorphous TiO_2[21,22] as well as anatase TiO_2[23–35] have attracted much attention due to their low cost, environmental friendliness, attractive theoretical specific capacity of 335 mAh g^{-1} and good electrochemical performance.

Challenges of pristine anatase TiO_2 are its low electric conductivity and the slow ion diffusion.[27] However, we recently reported the formation of metallic titanium upon initial sodiation, which explains the good rate capability of the pristine material after the initial activation process at low potentials.[24]

Downsizing the active material particles to nanoscale, which has already proven successful for active materials in lithium-ion batteries,[36,37] is another approach to further improve the electrochemical performance. In addition, various other strategies including doping of TiO_2,[23,38,39] carbon coatings, or the use of graphene as a conductive additive have been proposed to improve the performance of TiO_2 as negative electrode material.[18,28,34] Nevertheless, the use of graphene on industrial scale is still challenging as a cost effective and up-scaled synthesis

Dr. M. N. Tahir, Dr. M. Panthöfer, Prof. W. Tremel
Institute for Inorganic and Analytical Chemistry
University of Mainz
Duesbergweg 10-14, 55128 Mainz, Germany
Dr. B. Oschmann, Prof. R. Zentel
Institute for Organic Chemistry
University of Mainz
Duesbergweg 10-14, 55128 Mainz, Germany
E-mail: zentel@uni-mainz.de
Dr. B. Oschmann
Graduate School Materials Science in Mainz
Staudinger Weg 9, 55128 Mainz, Germany
Dr. D. Buchholz, X. Dou, Prof. S. Passerini
Helmholtz Institute Ulm (HIU)
Electrochemistry I
Helmholtzstr. 11, 89081 Ulm, Germany
E-mail: stefano.passerini@kit.edu
Dr. D. Buchholz, X. Dou, Prof. S. Passerini
Karlsruhe Institute of Technology (KIT)
P.O. Box 3640, 76021 Karlsruhe, Germany
Dr. I. Lieberwirth
Max Planck Institute for Polymer Research
Ackermannweg 10, 55128 Mainz, Germany

DOI: 10.1002/aenm.201501489

still needs to be established.[40] Instead, carbon coatings are known to be a promising method and successful strategy to improve the electrochemical performance of various materials.[27,29,30] Common strategies to obtain carbon-coated nanoparticles often involve at least three steps, starting with the synthesis of the inorganic particle followed by mixing of particles with a carbon precursor (for example glucose) and, finally, the pyrolysis of the latter at elevated temperature.[26,30,41,42] The major drawback related to this method is the solvent incompatibility of the oxide and carbon precursor components which often leads to phase separation (i.e., agglomeration) of the nanoparticles and ultimately in a rather inhomogeneous distribution of the carbon coating. Advanced strategies based on postfunctionalization include the binding of a carbon precursor polymer onto the nanoparticle which leads to the formation homogeneously coated particles.[43,44] This, consequently, leads to improved electrochemical performance. However, as it relies on a postfunctionalization strategy, it requires several synthetic steps for obtaining the final carbon-coated material, which leads to increasing cost and aggravated scale up.

To resolve these problems, we developed the synthesis of a carbon precursor, polymeric ligand coated TiO_2 nanoparticles using an in situ surface functionalization approach, which can be scaled up to the multigram range very easily. The carbon precursor block copolymer used as surface ligand consists of a well-graphitizable polyacrylonitrile (PAN) block and a hydroxamic acid anchor block, as hydroxamate units are reported to bind tightly to transition metals.[45,46] The block copolymer plays a dual role: (i) the surface chelating block (hydroxamate) controls the growth, size, and crystallinity of nanoparticles at the nucleation stage and ensures the binding of carbon precursor polymer to every nucleus and (ii) the graphitizable block shields the nanoparticles, controls their porosity and provides sufficiently extended electron pathways after pyrolysis. This synthetic strategy reduces the number of synthesis steps and yields TiO_2 nanoparticles with very small particle size (≈11 nm). This allows for smaller diffusion lengths while the carbon network maintains sufficient electrical conductivity. The impact of the particle size and the importance of the carbon coating are demonstrated by comparing the obtained carbon-coated TiO_2 anatase nanoparticles with uncoated material having comparable particle size (≈15 nm) and large carbon-coated particles (≈40 nm).

We believe that this work provides insight on the role of particle size and carbon-coating on the electrochemical performance of anatase TiO_2 (and metal oxide particles in general). The in situ surface functionalization method described here may be highly relevant for materials optimization and future studies. Most importantly, the carbon-coated anatase TiO_2 nanoparticles exhibit an extraordinary electrochemical performance in SIBs, combining high capacity, coulombic efficiency, capacity retention, and rate performance.

2. Results and Discussion

2.1. Synthesis and Characterization of Carbon-Coated TiO_2 Particles

A schematic illustration for the synthesis of the carbon-coated TiO_2 nanoparticles is shown in **Figure 1**. The block copolymer

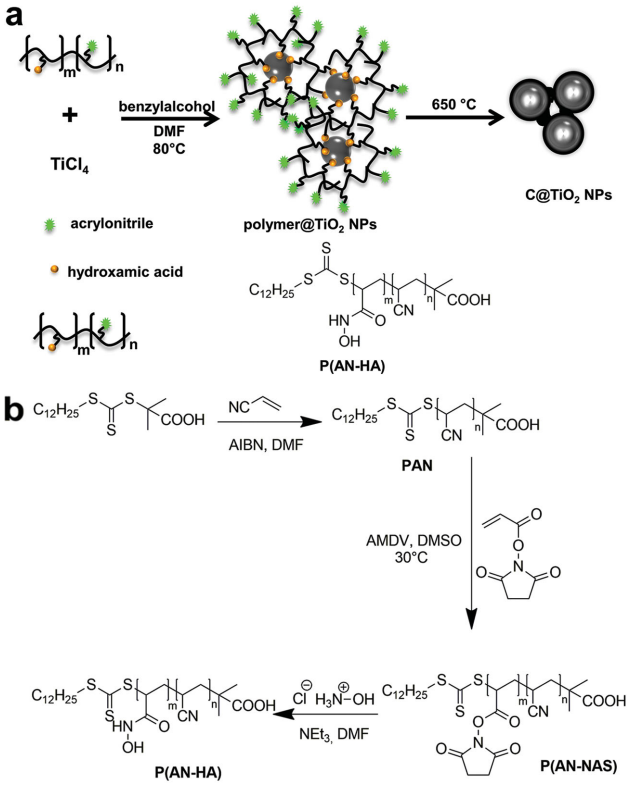

Figure 1. a) Schematic synthesis route for carbon-coated TiO_2 nanoparticles obtained by in situ polymer functionalization and b) synthesis route of the block copolymer.

contains an acrylonitrile block as carbon precursor moiety and a hydroxamic acid group as in situ chelating ligand to control the nucleation and growth process of the TiO_2 nanoparticles. Hydroxamic acid was chosen as coordinating surface anchor, as it is known to coordinate the transition metals cations on thin films.[45,47] However, to the best of our knowledge, it has not been used as an in situ anchor group to synthesize well crystalline metal oxide nanoparticles. Moreover, hydroxamate appears more attractive compared to the well-established catechol coordination chemistry applied previously[32,43,48,49] as it is not susceptible to oxidation.

The hydroxamic acid containing block copolymer was synthesized by reversible addition-fragmentation chain transfer (RAFT) polymerization. The synthesis scheme is illustrated in Figure 1b. As reported previously[43] the carbon precursor block consisting of polyacrylonitrile was synthesized in the first step. The average block length contained 80 repeat units as determined by NMR spectroscopy (see Figure S1, Supporting Information). In the next step, the hydroxamic acid anchor group was introduced using reactive ester chemistry. Therefore, *N*-acryloxysuccinimide (NAS) was used as a second monomer for the block copolymerization and PAN was used as macro-RAFT agent to obtain P(AN-*b*-NAS). The block length of the reactive ester was ≈31 repeat units, as estimated by NMR spectroscopy (see Figure S2, Supporting Information). Aminolysis of the reactive ester with hydroxylamine yielded the hydroxamic acid containing polymer poly(acrylonitrile-*b*-hydroxamic acid) (P(AN-*b*-HA) as confirmed by IR-spectroscopy (Figure S3a,

Supporting Information) and NMR spectroscopy (Figure S4, Supporting Information). As shown in Figure S3a (Supporting Information) the reactive ester band (1732 cm^{-1}) of NAS, observable prior to the aminolysis, is absent after aminolysis. An amide band (1648 cm^{-1}) and a hydroxyl band indicated the successful conversion. Furthermore, the polymer was characterized by size exclusion chromatography (SEC). Figure S3b (Supporting Information) shows the elugrams of polyacrylonitrile (Polydispersity Index (PDI): 1.20) and of P(AN-*b*-HA) (PDI: 1.28). After aminolysis the polymer still shows a rather low polydispersity, suggesting that no cross-linking occurred. The clean reaction was also demonstrated by the absence of ester bands, which might occur due to the alcoholysis of the hydroxyl group of hydroxylamine.

The resulting polymeric ligand was used as in situ functionalizing ligand to synthesize the carbon-coated TiO_2 nanoparticles using benzyl alcohol route. The synthesis of anatase TiO_2 nanocrystal using $TiCl_4$ as titanium precursor and benzyl alcohol both as solvent and oxygen donating molecules is a well established procedure.[50–52] However, in this present study hydroxamic acid (used as anchor group) binds to TiO_2 nuclei surfaces via bidentate chelation, which helps in stabilizing the phase pure anatase structure orienting the TiO_6 octahedron in a position to result in anatase instead of rutile formation.[53] Zhang and co-workers, for example, reported that bulky ligands capable of bidentate chelation resulted in anatase structure.[53] The acrylonitrile block can be graphitized by pyrolysis. The overall TiO_2 synthesis is based on a modified benzyl alcohol methodology reported by Niederberger et al.[52,54] As shown in Figure 1a, $TiCl_4$ and P(AN-*b*-HA) were solved in a benzyl alcohol/*N*,*N*-dimethylformamide (DMF) mixture, and the reaction mixture was stirred at 80 °C under inert conditions to obtain gram amounts of polymer-coated TiO_2 (see Figure S5, Supporting Information). The resulting particles were characterized by high resolution transmission electron microscopy (HRTEM), and corresponding images are shown in **Figure 2**a. The crystallinity of the TiO_2 anatase nanoparticles is apparent from the fast Fourier transform (FFT) and by the fringe spacing (≈0.35 nm). This is close to 0.352 nm, the reported value of the (101) lattice spacing for anatase TiO_2 (ICDD 00-001-5062). The average particle diameter is ≈11 nm. As mentioned above, the hydroxamate blocks, acting as bulky bidentate chelating ligands, bind to TiO_2 controlling the crystal growth. The powder X-ray diffraction (PXRD) (Figure 2b), in fact, confirms that the synthesized product is composed of pure, anatase phase crystals. In order to estimate the organic content of the as-synthesized particles, thermogravimetric analysis (TGA) was conducted. The total weight loss is 40 wt%, whereby two shoulders can be observed in the TGA data as shown in Figure S6a (Supporting Information). The first shoulder at around 250 °C is assigned to the presence of benzyl alcohol,[55] and the second shoulder at around 500 °C to the bound polymer.[43] The estimated polymer/TiO_2 weight ratio is 23:77. Furthermore, the IR spectrum of the hybrid material includes typical polymer bands, especially the nitrile group at 2246 cm^{-1} (see Figure S6b, Supporting Information). The hydroxyl band at 3200 cm^{-1} indicates the presence of benzyl alcohol, which is in agreement with the observation of the TGA data. Upon heat treatment at 650 °C, the polymer surrounding the particles can be transformed into a

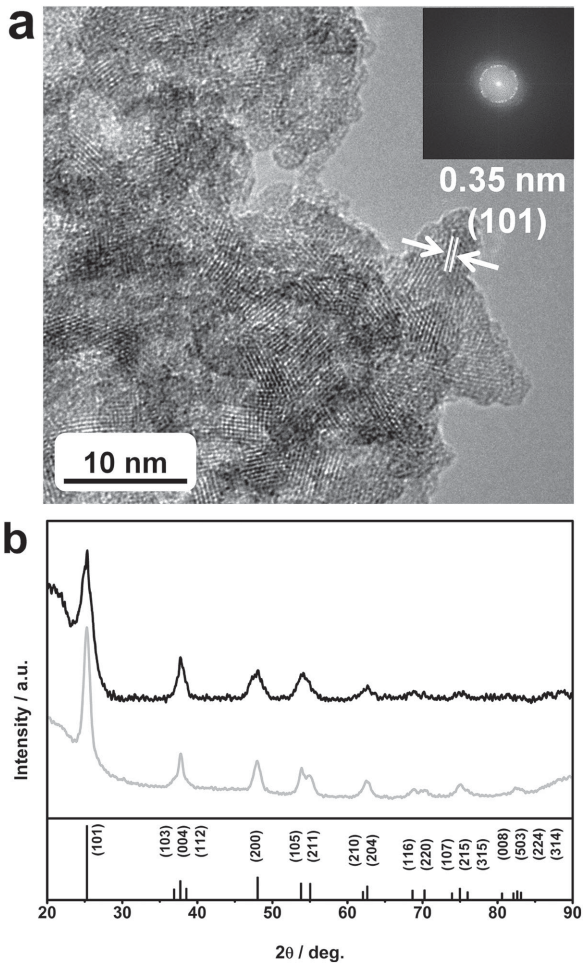

Figure 2. a) HRTEM image of as-synthesized TiO_2 particles with the FFT (inset) indicating a lattice spacing of 0.35 nm corresponding to the (101) reflection. b) PXRD pattern of as-synthesized TiO_2 particles (black) and carbon-coated TiO_2 particles (gray) with the JCPDS 01-071-1167 reference for anatase TiO_2 at the bottom.

carbonaceous shell. The content of organic material remaining from the carbonaceous residue, containing mainly carbon and nitrogen after pyrolysis, decreases to 12 wt% as shown by TGA (see **Figure 3**a). This is in good agreement with the results of a CHN elemental analysis, where a carbon content of 10.4 wt% and a nitrogen content of 1.4 wt% were determined. The presence of nitrogen can be attributed to an incomplete removal of nitrogen from the polyacrylonitrile. Raman spectroscopy (see Figure 3b) indicates the presence of carbonaceous material after pyrolysis due to the appearance of the D band at 1349 cm^{-1} and the G band at 1601 cm^{-1}. As demonstrated by PXRD (shown in Figure 2b) the anatase crystal structure remained after pyrolysis at 650 °C and no phase transformation was observed. Quantitative phase analysis based on the PXRD data (Figure S7, Supporting Information) for a bulk sample revealed the sizes of the individual crystalline domains within these particles to be 3.0 nm (as determined by full pattern profile fits) according to established structure models ("Rietveld refinement"), thus indicating a polycrystalline nature of the single particles. Reflection profiles were generated by applying the fundamental parameter

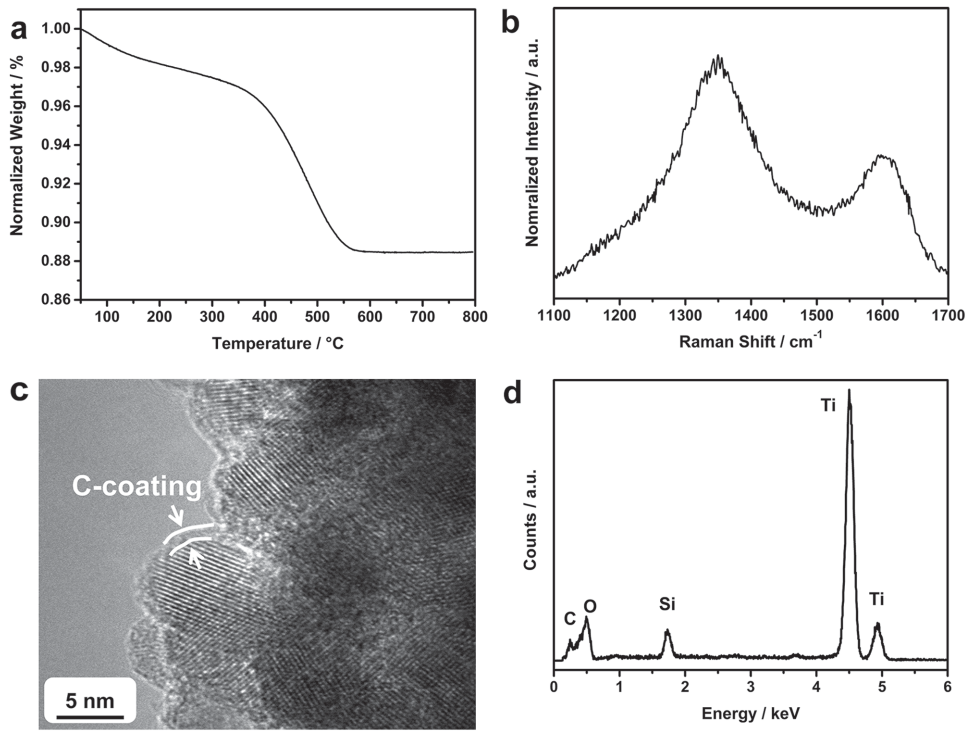

Figure 3. a) TGA data of 11 nm sized carbon-coated TiO_2 particles measured under oxygen atmosphere. b) Raman spectrum of carbon-coated TiO_2 particles. c) HRTEM image and d) EDX data corresponding to the area scan indicated in Figure S7 (Supporting Information) of carbon-coated TiO_2 particles.

approach as implemented in TOPAS Academic V5 program. The specific surface area was determined after pyrolysis by the Brunauer–Emmet–Teller (BET) method, revealing a value of 119.8 m^2 g^{-1}. HRTEM images show a thin amorphous layer (≈1–2 nm thickness) around the inorganic particles (Figure 3c). Finally, an energy dispersive X-ray (EDX) area scan shows the presence of a surface carbon layer on the inorganic particles (Figure 3d and Figure S8, Supporting Information).

It should be pointed out that in this section only the carbon-coated TiO_2 particles, not containing any additional carbon additive (Super C65), were investigated in order to allow a reasonable characterization of the TiO_2 particles as well as the carbon coating. However, for the application and investigation of this material in SIBs the conductive carbon particles were added prior to the thermal annealing of the hybrid material (see the Experimental Section) according to our previous procedures.[43]

2.2. Electrochemical Characterization of Carbon-Coated TiO_2 Nanoparticles

The electrochemical behavior of the carbon-coated TiO_2 particles with a diameter of 11 nm (abbreviated as C-TiO_2 (11 nm) in the sequel) was investigated initially by cyclic voltammetry in the voltage range from 0.05 to 2.0 V at a scan rate of 0.1 mV s^{-1} (**Figure 4**). The cathodic peak of the first scan at ≈0.8 V can be attributed to the formation of the solid electrolyte interface due to reductive electrolyte decomposition. For nanocrystalline anatase TiO_2 the current flowing at lower voltages of 0.3 V can be assigned to the partial conversion of TiO_2 to metallic titanium and sodium peroxide as well as to the reversible sodiation of TiO_2 resulting in the formation of sodium titanate.[24] During the first anodic sweep a broad peak in the range of 0.5–1.1 V is observed, which can be assigned to the Ti^{3+}/Ti^{4+} redox couple.[24] In the following sweeps, broad but highly reversible cathodic and anodic peaks, with slightly increasing intensities, are observed in the range from 0.55 to 1.2 V and 0.6 to 1.3 V, respectively. Such a (de-)sodiation mechanism is in accordance with other works[56,57] although it should be noted that it is also discussed controversially. The preservation of anatase TiO_2 structure throughout complete cycling, e.g., has been observed for nanorods and nanofibers of anatase TiO_2. The (de-)sodiation process of other TiO_2 polymorphs may, of course, also differ. For example, Usui et al. observed unchanged phase throughout cycling for rutile TiO_2.[38]

To investigate the effect of particle size as well as the presence of the carbon coating on the electrochemical performance, the C-TiO_2 (11 nm) was subjected to a C-rate test and compared with two reference materials: (i) carbon-coated anatase TiO_2 particles with diameters of 40 nm (see the Experimental Section and scanning electron microscopy (SEM) image in Figure S9, Supporting Information, BET surface area: 41.4 m^2 g^{-1}) (C-TiO_2 (40 nm)) and (ii) uncoated TiO_2 particles with a particle diameter of 15 nm, as determined by SEM and HRTEM (Figures S9a and S10a, Supporting Information, BET surface area: 91.7 m^2 g^{-1}), abbreviated as TiO_2 (15 nm). Individual crystallite domain sizes were obtained by Rietveld refinement and are determined to be ≈5.3 nm corresponding to a polycrystalline nature as also observed for C-TiO_2 (11 nm).[58,59] The crystallite size of C-TiO_2 (40 nm) is 36 nm (see Rietveld

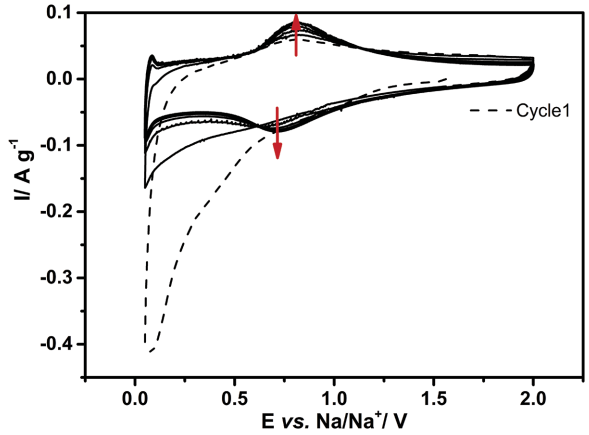

Figure 4. Cyclic voltammogram of C-TiO_2 (11 nm) with a scan rate of 0.1 mV s^{-1}. Shown cycles: 1, 2, 5, 10, 15, and 20. Reversing potentials: 0.05 and 2.0 V (vs Na/Na^+).

refinement in Figure S11, Supporting Information). Thus, the trend of crystallite size correlates with the one of particle size.

Electrochemical impedance spectroscopy (EIS) was performed for all three samples (Figure S12, Supporting Information, EIS data after first charge at 0.1 C). Obviously, the carbon-coated samples exhibit a lower charge transfer resistance due to the increased conductivity in the presence of the carbon coating.

The results of the C-rate test are reported in **Figure 5**. We note that the specific capacities for C-TiO_2 (40 nm) and C-TiO_2 (11 nm) reported in **Figures** 5 and **6** and Figure S11 (Supporting Information) are based on the weight of TiO_2 only and do not include the weight of carbon from the carbon coating and conductive additive.

In the first cycle a lower specific current of 0.02C (6.7 mA g^{-1}) was applied to ensure the complete activation of the TiO_2 anatase nanoparticles, which, in turn, improves the electrochemical performance in terms of specific capacity and coulombic efficiency according to our previous results.[19,24] In fact, lower specific capacities were obtained when the first cycle was performed at 0.1 C (Figure S13, Supporting Information). The specific charge capacity for the smaller particles, i.e., for C-TiO_2 (11 nm) and TiO_2 (15 nm) are 267 and 233 mAh g^{-1}, respectively, and thus significantly higher compared to the specific charge capacity of C-TiO_2 (40 nm) (209 mAh g^{-1}). Considering the weight percent (see the Experimental Section) and capacity contribution of the additionally added conductive carbon particles (75 mAh g^{-1}) as well as the carbon coating (125 mAh g^{-1}) reported in our previous studies[24,32] enables the determination of the specific capacities related to electrochemical redox activity of TiO_2 only. This implies that electrolyte decomposition and possible side reactions during the desodiation process are neglected. For C-TiO_2 (40 nm) only ≈189 mAh g^{-1} (0.56 eq. Na^+ per formula unit TiO_2) can be attributed to the titanium redox process during the first charge, whereas higher capacities can be obtained for uncoated TiO_2 (15 nm) (214 mAh g^{-1}, 0.64 eq. Na^+) and C-TiO_2 (11 nm) with (242 mAh g^{-1}, 0.72 eq. Na^+). This, indeed, nicely illustrates that higher degrees of reversible sodium (de-)insertion are possible if the active material particles are downsized to small particles with even small crystallite size, which is in accordance with the reported effect of particle size on the electrochemical behavior of anatase TiO_2 as negative electrode material in LIBs.[60] Most importantly, the presence

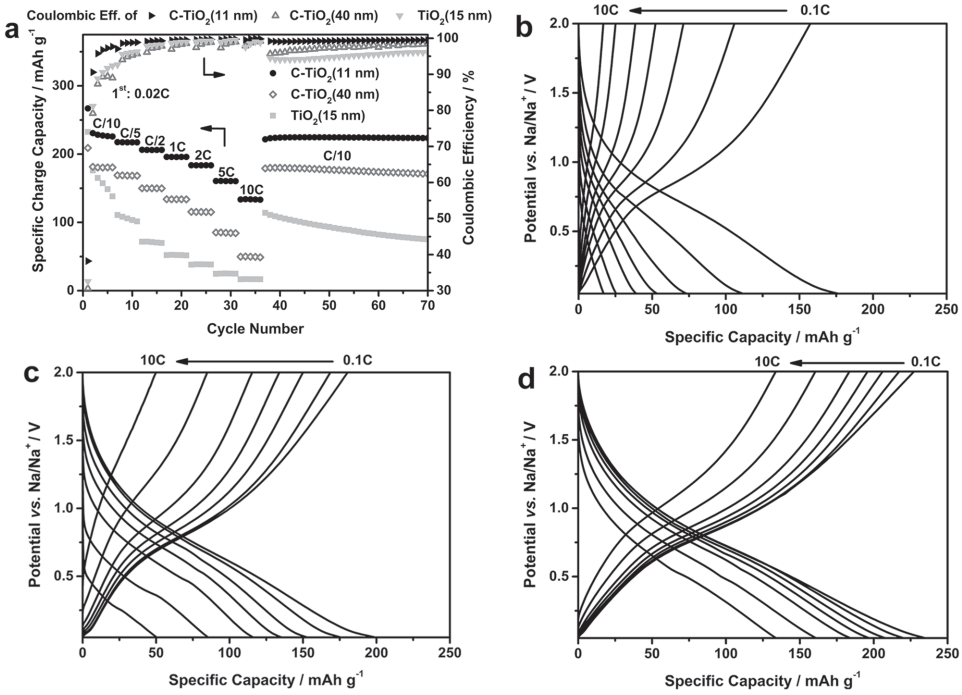

Figure 5. a) Cycling performance of TiO_2 (15 nm), C-TiO_2 (40 nm), and C-TiO_2 (11 nm) at various C-rates and corresponding selected potential profiles of b) TiO_2 (15 nm), c) C-TiO_2 (40 nm), and d) C-TiO_2 (11 nm) at 0.1 C (4th cycle), 0.2 C (9th cycle), 0.5 C (14th cycle), 1 C (19th cycle), 2 C (24th cycle), 5 C (29th cycle), and 10 C (34th cycle). Cut-off potentials: 0.05 and 2.0 V.

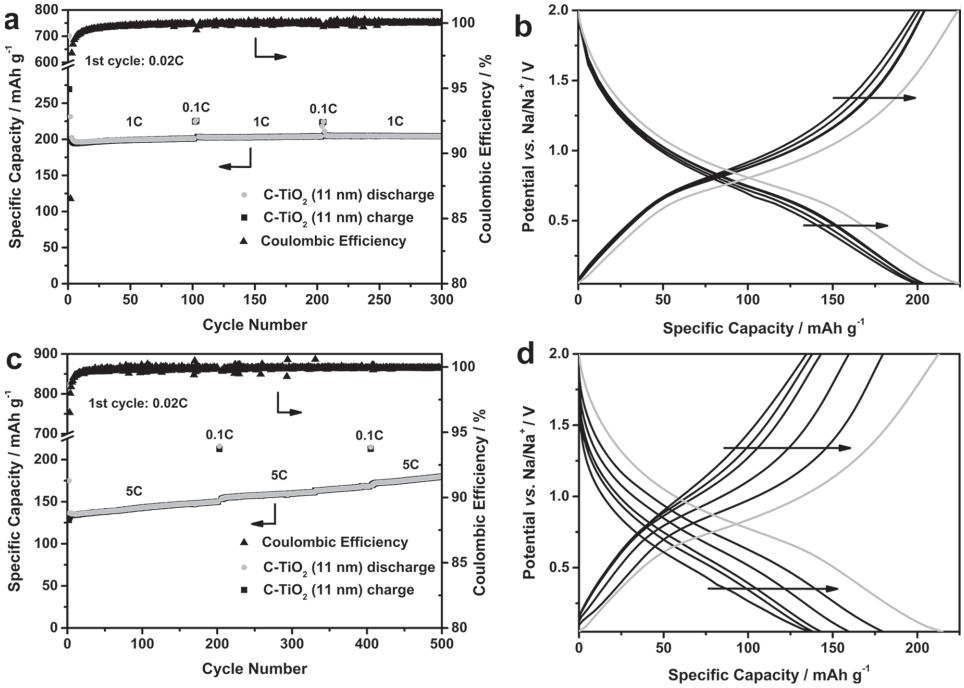

Figure 6. a) Long-term cycling performance of C-TiO_2 (11 nm) at 1 C and b) selected potential profiles of cycle 5, 50, 100, 200, and 300 at 1 C. Cycle 205 at 0.1 C (fingerprint) is shown in gray color. c) Long-term cycling of C-TiO_2 (11 nm) at 5 C and d) corresponding potential profiles of cycle 5, 50, 100, 300, and 500 at 5 C. Cycle 405 at 0.1 C (fingerprint) is shown in gray color. Cut-off potentials: 0.05 and 2.0 V.

of the carbon coating increases the ability for the reversible uptake/release of large contents of Na^+ upon cycling. It should be pointed out that the degree of reversible (de-)sodiation (0.72 eq. of Na^+ per formula unit TiO_2) is limited by the activation process in the initial sodiation of nanocrystalline anatase TiO_2, which leads to the partial and irreversible decomposition of TiO_2 and reduction of Ti^{4+} to metallic titanium, which no longer participates in the electrochemical redox process.[24] As a consequence of the above irreversible processes, the first cycle coulombic efficiency for all three materials is rather low and only ≈38.2%, 32.6%, and 30.6% for C-TiO_2 (11 nm), C-TiO_2 (40 nm), and TiO_2 (15 nm), respectively. Identifying methods to compensate for such high inefficiency represents a major challenge to allow the application of this material class in Na–ion cells, which are presently under development in our laboratories.

Further cycling at different current rates reveals a strong capacity fading for the uncoated TiO_2 (15 nm) (Figure 5a), which can be explained by continuous solid electrolyte interphase (SEI) formation. The low average coulombic efficiency of 94.7%, indeed, indicates for the presence of a parasitic side reaction, e.g., continuous electrolyte decomposition. In contrast, the larger carbon-coated nanoparticles C-TiO_2 (40 nm) show a more stable cycling performance. As a matter of fact, higher specific capacities compared to uncoated TiO_2 (15 nm) material were delivered from the fifth cycle onward.

Most impressive is, however, the electrochemical performance of C-TiO_2 (11 nm) in comparison with C-TiO_2 (40 nm) and TiO_2 (15 nm). In fact, C-TiO_2 (11 nm) former delivers the highest capacity at all applied C-rates as well as the most stable cycling performance. For instance, reversible charge capacities of 227, 196, and 134 mAh g^{-1} can be obtained at 0.1 C (33.5 mA g^{-1}), 1C (335 mA g^{-1}), and 10C (3.35 A g^{-1}), respectively. At the same rates, C-TiO_2 (40 nm) delivers only 180, 134, and 51 mAh g^{-1} and uncoated TiO_2 (15 nm) delivers only 157, 52, and 17 mAh g^{-1} at the corresponding current rates. Besides the extraordinary C-rate performance, C-TiO_2 (11 nm) also exhibits the highest capacity retention of 96.9% after 70 cycles (vs 2nd cycle) compared to 94.2% for C-TiO_2 (40 nm) and only 42.8% for TiO_2 (15 nm). The different capacity retention goes along with the trend of the average coulombic efficiency, which at low (0.1 C) current rate, e.g., between cycle 40 and 70, ranges between 99.0% and 99.5%, 97.5% and 98.5%, and 94.5% and 96.0% for C-TiO_2 (11 nm), C-TiO_2 (40 nm), and TiO_2 (15 nm), respectively.

Selected potential profiles, obtained at different C-rates, are shown in Figure 5b–d for TiO_2 (15 nm), C-TiO_2 (40 nm), and C-TiO_2 (11 nm), respectively. Evaluation clearly reveals the superior C-rate performance of C-TiO_2 (11 nm) as the potential profiles are less sloping and shifting at elevated currents while for the other two materials the evolution of large overpotentials is apparent. This is additionally evidenced by the voltage region from 0.75 to 1.25 V during desodiation, being much more pronounced in case of C-TiO_2 (11 nm) for all applied C-rates.

The superior electrochemical performance of C-TiO_2 (11 nm) prompted a more detailed investigation with respect to the long-term cyclability (Figure 6). After a certain number of cycles at high current rate (1 C or 5 C), two "fingerprint" cycles at 0.1 C were performed to verify the good electrode performance and absence of active material degradation upon long-term cycling as well as cycling at elevated current rates. As shown in Figure S13 (Supporting Information) C-TiO_2 (11 nm)

exhibits a very stable cycling performance when applied to an extended cycling at several C-rates ranging from 0.1 C, 1 C to 5 C. Figure 6a shows the remarkably stable long-term cycling performance of C-TiO_2 (11 nm) at 1 C, in which the capacity even increases slightly (200 mAh g^{-1} in the 2nd vs 204 mAh g^{-1} in the 300th cycle) as also visible in the potential profiles in Figure 6b. Additionally, the coulombic efficiency increases from 86.5% (second cycle) to a very high average value of 99.8%.

A remarkable intrinsic feature of this material is the improving energy efficiency upon cycling which is related to the incomplete initial activation process at low potentials as shown in our previous work but as also apparent in the long-term cycling in Figure 6c,d.[24] In fact, increasing the C-rate to 5 C still results in highly reversible cycling, whereby the effect of increasing capacity upon cycling is even more pronounced compared to the cycling at 1 C. A charge capacity of 128 mAh g^{-1} is delivered in the 2nd cycle which subsequently increases to ≈180 mAh g^{-1} after 500 cycles. The capacity increase is observed especially after the "fingerprint" cycles, which, indeed, indicates an incomplete initial activation at low potential after the first cycle at 0.02 C. In any case, it should be highlighted that C-TiO_2 (11 nm) delivers an excellent electrochemical long-term performance at low and very high current rates even under demanding conditions like a C-rate test.

3. Conclusion

The synthesis of carbon-coated 11 nm TiO_2 nanoparticles via an in situ functionalization approach is reported. This method relies on the use of an anchoring block copolymer carbon precursor, which, after combustion, results in homogeneously carbon-coated TiO_2 nanoparticles. The process can easily be upscaled to the multigram range and readily be applied to other materials.

The beneficial impact of small particle and crystallite sizes and the herein developed carbon coating for the electrochemical performance of anatase TiO_2 is clearly demonstrated by comparison with reference materials. The final carbon-coated TiO_2 is capable of reversibly accommodating 0.72 eq. Na^+ per formula unit TiO_2 at low current rate (0.02 C), which certainly is one of the highest values reported so far. In addition, the material reveals an extraordinary electrochemical performance in sodium-metal half cells with very high rate capability (134 mAh g^{-1} at 10 C (3.35 A g^{-1})), high reversible capacity at low current rates (≈227 mAh g^{-1} at 0.1 C), high average coulombic efficiency (≈99.5%) and full capacity retention between 2nd and 300th cycle at 1 C. Despite this excellent electrochemical performance, the low first cycle coulombic efficiency still represents the biggest challenge to be overcome (e.g., via appropriate electrolyte additives, optimization of particle size and shape, or the use of sacrificial salts[61,62] in order to allow for the application such materials in powerful Na–ion cells.

4. Experimental Section

Synthetic and Structural Characterization: NMR spectroscopy was conducted with a Bruker ARX 400. Fourier transform infrared (FTIR) spectroscopy was performed on a Jasco FT/IR 4100 spectrometer with an attenuated total reflectance (ATR) unit. SEC was carried out using a solution of 3 g L^{-1} K^+TFA^- in hexafluoroisopropanol as eluent at 40 °C. The stationary phase in the columns consists of modified silica. The utilized detector was a refractive index detector (JASCO G1362A RID) and the calculation of the molecular weights was conducted using a calibration with polymethylmethacrylate (PMMA) standards. HRTEM, scanning transmission electron microscopy, and energy dispersive X-ray spectroscopy was performed on a Tecnai F 20 (FEI). Scanning electron microscopy was conducted using ZEISS Auriga. X-ray diffraction was performed on a Siemens D 5000 (Cu-K-alpha radiation) for C-TiO_2 (11 nm) and on a Bruker D8 Advance diffractometer equipped with Cu-Kα radiation source (wavelength of 1.54056 Å) for noncarbon-coated TiO_2 (15 nm). TGA was conducted on a Perkin Elmer Pyris 6 instrument under oxygen atmosphere. A Horiba Jobin Y LabRAM HR Spectrometer with a frequency doubled neodymium- doped yttrium aluminum garnet (Nd:YAG) laser was utilized to perform Raman spectroscopy. The specific surface area was measured by nitrogen adsorption and calculated according to the BET theory (Micrometrics ASAP 2020). EIS was carried out by means of a Solartron 1250 Frequency Response Analyzer with either an EG&G potentiostat/galvanostat model 273 or a Solartron 1286 electrochemical interface in a two-electrode configuration. The frequency ranged from 1 MHz to 10 mHz. All EIS studies were carried out in the charged (desodiated) state.

Synthesis of P(AN-b-HA): The reactive ester NAS and 2-dodecylsulfanylthiocarbonylsulfanyl-2-methyl propionic acid (DMP), which was used as a chain transfer agent, were synthesized following procedure described already in literature.[63,64] P(AN-*b*-NAS) was synthesized following a previously reported method.[43] Briefly, acrylonitrile (AN, Merck, purified by destillation), DMP, and α,α'-azoisobutyronitrile (Sigma-Aldrich, recrystallized from diethylether) were dissolved dry DMF 99.8% (Acros Organics). After degassing by freeze–pump–thaw cycles, the reaction mixture was stirred 7 h at 70 °C. After purification by precipitation in methanol PAN was used as a macro-CTA, NAS as a monomer, 2,2-azobis(4-methoxy-2,4-dimethylvaleronitrile) (Sigma-Aldrich) as an initiator and dimethyl sulfoxide (DMSO 99.9%, Acros Organics) as a solvent. After stirring for 48 h at room temperature the polymer was worked up by precipitation in methanol.

IR: ν = 2941 (w, CH), 2240 (w, –CN), 1731 (s, C=O, reactive ester), 1203 (s), 1045 (s), 951 (w), 812 (w) cm^{-1}.

^{1}H NMR (400 MHz, DMSO-d_6, δ) [ppm]: 3.19 (bs, 111, C*H* of polymer backbone), 2.79 (bs, 125, CH_2–CH_2 of N-Hydroxysuccinimide (NHS)-group), 2.03 (bs, 279, CH_2 of polymer backbone), 1.23 (m, CTA dodecyl chain), 0.85 (t, 3, dodecyl-CH_3 of CTA).

SEC (eluent: hexafluoroisopropanol, HFIP): 10 300 g mol^{-1}, PDI: 1.30

P(AN-*b*-NAS) (1 eq.), hydroxylamine hydrochloride (40 eq.), and triethylamine (40 eq.) are dissolved in DMF and stirred over night at room temperature. The polymer was purified by precipitation in methanol to obtain P(AN-*b*-HA). The yield was ≈85 wt%.

IR: ν = 3260 (w, –OH), 2925 (w, CH), 2240 (w, –CN), 1648 (s, C=O, amide), 1386 (m), 1096 (m) cm^{-1}.

^{1}H NMR (400 MHz, DMSO-d_6, δ) [ppm]: 3.34 (bs, C*H*CONHOH), 3.14 (bs, C*H*CN), 2.04 (bs, CH_2-CHCN), 1.55 (CH_2–CHCONHOH), 1.23 (m, CTA dodecyl chain), 0.85 (t, CTA-CH_3).

SEC (eluent: HFIP): 14 300 g mol^{-1}, PDI: 1.29.

Synthesis of In Situ Functionalized TiO_2 Nanoparticles: 200 mg of hydroxamic acid containing polymer ligand was dissolved in 10 mL of DMF and added to 30 mL of benzyl alcohol (Sigma-Aldrich). The polymer solution was heated to 80 °C and degassed under vacuum for 5 min. The flask was then filled with argon and kept at this temperature. 1.6 mL of $TiCl_4$ (Sigma-Aldrich) was slowly injected through the septum into the hydroxamic acid containing polymer containing solution under vigorous stirring at 80 °C. With continuous stirring the solution was kept at 80 °C for 72 h. The resulting brown suspension was centrifuged and the precipitate was thoroughly washed twice with $CHCl_3$. The product was dried under vacuum at room temperature.

Pyrolysis of Polymer-Coated TiO_2 Nanoparticles: Polymer-coated TiO_2 nanoparticles were pyrolyzed in two steps. First, the powder was

heated up to 300 °C with 5 °C min^{-1} as a heating rate and kept at this temperature for 240 min. Afterward the temperature was increased to 650 °C with 5 °C min^{-1} and kept at this temperature for 60 min. For the synthetic characterization no carbon particles were added prior to pyrolysis to enable a reasonable characterization of the coating.

However, for the samples subjected to electrochemical tests, the conductive carbon particles (Super C 65) were added to the polymer-coated particles and the mixture was manually ground for 30 min prior pyrolysis (same temperature program), in accordance with our previous reports.[37,43] The TiO_2 (pure, polymer coated): Super C65 weight ratio was fixed to 84:16. After pyrolysis thermogravimetric analysis under oxygen enabled the determination of the final weight percentage share of TiO_2 (73 wt%) as well as carbon originating from the coating (13 wt%, degradation at 450 °C) and from the conductive agent (14 wt%, degradation at 650 °C) as shown in Figure S14 (Supporting Information).

Synthesis of TiO_2 Reference Samples: TiO_2 particles with a size of ≈40 nm (Sigma-Aldrich, used as received) were coated with P(AN-*b*-HA), mixed with carbon particles and pyrolyzed under the same conditions as described for the in situ functionalized particles. The resulting composite had a weight percentage share of TiO_2: carbon coating: carbon particle of 73:9:16 as determined by TGA. Uncoated TiO_2 particles with a size of ≈15 nm were synthesized by a method reported previously.[54] Briefly, benzyl alcohol (20 mL) was sealed in a Schlenk flask (100 mL) in a glovebox and was removed from the glovebox. $TiCl_4$ (0.8 mL) was slowly injected through the septum to the solution of ligand in benzyl alcohol under vigorous stirring at room temperature. With continuous stirring the solution was heated to 80 °C for 24 h under Ar conditions. The resulting white suspension was centrifuged, and the precipitate was thoroughly washed twice with $CHCl_3$. The product was dried in air at room temperature.

Electrochemical Characterization: For the electrochemical characterization, anatase TiO_2 electrodes were prepared having a final composition of 65 wt% TiO_2, 25 wt% carbon (accounting for the carbon present in the TiO_2 particles and the conductive agent (SuperC65, IMERYS, Switzerland)), and 10 wt% PVdF binder (Solef 5130) dissolved in N-methyl-2-pyrrolidone (NMP). In consequence, with respect to the weight ratio of TiO_2: carbon coating: conductive agent: PVdF, electrodes of C-TiO_2 (11 nm size) had a composition of 65:12:13:10; electrodes of C-TiO_2 (40 nm size) a composition of 65:9:16:10, and the uncoated TiO_2 (15 nm size) material a composition of 65:0:25:10. For C-TiO_2 (11 nm) and C-TiO_2 (40 nm), the composite materials containing carbon-coated TiO_2 and Super C65 particles (added prior to pyrolysis) were simply mixed with 10 wt% PVdF (solution in NMP). In case of TiO_2 (15 nm), the pristine TiO_2 particles were mixed with Super C65 (25 wt%) and 10 wt% PVdF (solution in NMP) just before slurry fabrication. All slurries were homogenized by means of ball milling (Vario Planetary Mill Pulverisette 4, Fritsch) and then cast on dendritic copper foil (Schlenk) with a wet film thickness of 120 µm. After drying at ambient temperature overnight, disc electrodes (Ø = 12 mm) were punched and further dried at 120 °C under vacuum for 24 h. The average active material mass loading (of TiO_2 only) of C-TiO_2 (11 nm diameter), C-TiO_2 (40 nm diameter), and uncoated TiO_2 (15 nm diameter) was between 1.2 and 1.5, 1.8 and 1.2 mg cm^{-2}, respectively.

Three-electrode Swagelok cells were assembled in a glove box (MBraun, Germany) with a water and oxygen content less than 0.1 ppm. A sheet of Whatman glass fiber was used as separator which was drenched with a 1 M solution of $NaClO_4$ (98% Sigma-Aldrich) solved in a 1:1 mixture (by volume) of ethylene carbonate (UBE) and propylene carbonate (Sigma-Aldrich). Sodium metal (99.8%, ACROS ORGANICS) was used as counter and reference electrode. Thus, all given potentials in this paper refer to the Na/Na^+ reference couple. Cyclic voltammetry and galvanostatic cycling were performed with a VMP3 Potentiostat in the voltage range of 0.05 and 2.0 V at a scan rate of 0.1 mV s^{-1} (BIOLOGIC) and a Maccor Battery Tester 4300, respectively. All electrochemical studies were performed at 20 ± 2 °C. An applied current rate of 1C corresponds to a specific current of 335 mA g^{-1} based on the weight of TiO_2 only.

Supporting Information

Supporting Information is available from the Wiley Online Library or from the author.

Acknowledgements

M.N.T., B.O., and D.B. contributed equally to this work. The research leading to these results received funding from the European Union Seventh Framework Programme (FP7/2007-2013) under Grant Agreement No. 608621. B.O. would like to thank the graduate school MAINZ and is a recipient of the fellowship through the Excellence Initiative (Deutsche Forschungsgemeinschaft (DFG)/ Graduiertenschule (GSC) 266). All authors would like to thank Dr. Jan von Zamory for SEM measurements. Furthermore, the authors would like to thank Dr. Liming Wu for helpful discussions.

Received: July 23, 2015
Revised: October 12, 2015
Published online: December 7, 2015

[1] J.-M. Tarascon, M. Armand, *Nature* **2001**, *414*, 359.
[2] P. W. Gruber, P. A. Medina, G. A. Keoleian, S. E. Kesler, M. P. Everson, T. J. Wallington, *J. Ind. Ecol.* **2011**, *15*, 760.
[3] E. Tzimas, *Critical Materials in Energy Technologies, SETIS Materials for Energy* **2015**.
[4] F. Klein, B. Jache, A. Bhide, P. Adelhelm, *Phys. Chem. Chem. Phys.* **2013**, *15*, 15876.
[5] K. Zhang, Z. Hu, X. Liu, Z. Tao, J. Chen, *Adv. Mater.* **2015**, *27*, 3305.
[6] J. W. Wang, X. H. Liu, S. X. Mao, J. Y. Huang, *Nano Lett.* **2012**, *12*, 5897.
[7] L. D. Ellis, T. D. Hatchard, M. N. Obrovac, *J. Electrochem. Soc.* **2012**, *159*, A1801.
[8] S.-M. Oh, S.-T. Myung, M.-W. Jang, B. Scrosati, J. Hassoun, Y.-K. Sun, *Phys. Chem. Chem. Phys.* **2013**, *15*, 3827.
[9] Y. Zhu, X. Han, Y. Xu, Y. Liu, S. Zheng, K. Xu, L. Hu, C. Wang, *ACS Nano* **2013**, *7*, 6378.
[10] A. Darwiche, C. Marino, M. T. Sougrati, B. Fraisse, L. Stievano, L. Monconduit, *J. Am. Chem. Soc.* **2012**, *134*, 20805.
[11] L. Wu, X. Hu, J. Qian, F. Pei, F. Wu, R. Mao, X. Ai, H. X. Yang, Y. Cao, *Energy Environ. Sci.* **2014**, *7*, 323.
[12] S. Komaba, W. Murata, T. Ishikawa, N. Yabuuchi, T. Ozeki, T. Nakayama, A. Ogata, K. Gotoh, K. Fujiwara, *Adv. Funct. Mater.* **2011**, *21*, 3859.
[13] A. Ponrouch, A. Goñi, M. R. Palacín, *Electrochem. Commun.* **2013**, *27*, 85.
[14] Y. Cao, L. Xiao, M. L. Sushko, W. Wang, B. Schwenzer, J. Xiao, Z. Nie, L. V. Saraf, Z. Yang, J. Liu, *Nano Lett.* **2012**, *12*, 3783.
[15] B. Jache, P. Adelhelm, *Angew. Chem. Int. Ed.* **2014**, *53*, 10169.
[16] H. Pan, X. Lu, X. Yu, Y.-S. Hu, H. Li, X.-Q. Yang, L. Chen, *Adv. Energy Mater.* **2013**, *3*, 1186.
[17] P. Senguttuvan, G. Rousse, V. Seznec, J.-M. Tarascon, M. Palacín, *Chem. Mater.* **2011**, *23*, 4109.
[18] C. Chen, Y. Wen, X. Hu, X. Ji, M. Yan, L. Mai, P. Hu, B. Shan, Y. Huang, *Nat. Commun.* **2015**, *6*, 6929.
[19] L. Wu, D. Bresser, D. Buchholz, S. Passerini, *J. Electrochem. Soc.* **2014**, *162*, A3052.
[20] J. P. Huang, D. D. Yuan, H. Z. Zhang, Y. L. Cao, G. R. Li, H. X. Yang, X. P. Gao, *RSC Adv.* **2013**, *3*, 12593.
[21] Z. Bi, M. P. Paranthaman, P. A. Menchhofer, R. R. Dehoff, C. A. Bridges, M. Chi, B. Guo, X.-G. Sun, S. Dai, *J. Power Sources* **2013**, *222*, 461.

[22] H. Xiong, M. D. Slater, M. Balasubramanian, C. S. Johnson, T. Rajh, *J. Phys. Chem. Lett.* **2011**, *2*, 2560.
[23] X. Yang, C. Wang, Y. Yang, Y. Zhang, X. Jia, J. Chen, X. Ji, *J. Mater. Chem. A* **2015**, *3*, 8800.
[24] L. Wu, D. Bresser, D. Buchholz, G. Giffin, C. R. Castro, A. Ochel, S. Passerini, *Adv. Energy Mater.* **2015**, *5*, 1401142.
[25] L. Wu, D. Buchholz, D. Bresser, L. G. Chagas, S. Passerini, *J. Power Sources* **2014**, *251*, 379.
[26] K.-T. Kim, G. Ali, K. Y. Chung, C. S. Yoon, H. Yashiro, Y.-K. Sun, J. Lu, K. Amine, S.-T. Myung, *Nano Lett.* **2014**, *14*, 416.
[27] Y. Yang, X. Ji, M. Jing, H. Hou, Y. Zhu, L. Fang, X. Yang, Q. Chen, C. E. Banks, *J. Mater. Chem. A* **2015**, *3*, 5648.
[28] G. Qin, X. Zhang, C. Wang, *J. Mater. Chem. A* **2014**, *2*, 12449.
[29] J. Lee, Y.-M. Chen, Y. Zhu, B. D. Vogt, *ACS Appl. Mater. Interfaces* **2014**, *6*, 21011.
[30] Y. Ge, H. Jiang, J. Zhu, Y. Lu, C. Chen, Y. Hu, Y. Qiu, X. Zhang, *Electrochim. Acta* **2015**, *157*, 142.
[31] S.-M. Oh, J.-Y. Hwang, C. S. Yoon, J. Lu, K. Amine, I. Belharouak, Y.-K. Sun, *ACS Appl. Mater. Interfaces* **2014**, *6*, 11295.
[32] D. Bresser, B. Oschmann, M. N. Tahir, F. Mueller, I. Lieberwirth, W. Tremel, R. Zentel, S. Passerini, *J. Electrochem. Soc.* **2015**, *162*, A3013.
[33] Y. Xu, E. M. Lotfabad, H. Wang, B. Farbod, Z. Xu, A. Kohandehghan, D. Mitlin, *Chem. Commun.* **2013**, *49*, 8973.
[34] H. A. Cha, H. M. Jeong, J. K. Kang, *J. Mater. Chem. A* **2014**, *2*, 5182.
[35] J. R. Gonzalez, R. Alcantara, F. Nacimiento, G. F. Ortiz, J. L. Tirado, *J. Electrochem. Soc.* **2014**, *162*, A3007.
[36] A. S. Aricò, P. Bruce, B. Scrosati, J.-M. Tarascon, W. van Schalkwijk, *Nat. Mater.* **2005**, *4*, 366.
[37] D. Bresser, E. Paillard, M. Copley, P. Bishop, M. Winter, S. Passerini, *J. Power Sources* **2012**, *219*, 217.
[38] H. Usui, S. Yoshioka, K. Wasada, M. Shimizu, H. Sakaguchi, *ACS Appl. Mater. Interfaces* **2015**, *7*, 6567.
[39] D. Yan, C. Yu, Y. Bai, W. Zhang, T. Chen, B. Hu, Z. Sun, L. Pan, *Chem. Commun.* **2015**, *51*, 8261.
[40] R. Raccichini, A. Varzi, S. Passerini, B. Scrosati, *Nat. Mater.* **2014**, *14*, 271.
[41] D. Bresser, E. Paillard, R. Kloepsch, S. Krueger, M. Fiedler, R. Schmitz, D. Baither, M. Winter, S. Passerini, *Adv. Energy Mater.* **2013**, *3*, 513.
[42] S. Jeong, D. Bresser, D. Buchholz, M. Winter, S. Passerini, *J. Power Sources* **2013**, *235*, 220.
[43] B. Oschmann, D. Bresser, M. N. Tahir, K. Fischer, W. Tremel, S. Passerini, R. Zentel, *Macromol. Rapid Commun.* **2013**, *34*, 1693.
[44] B. Oschmann, M. N. Tahir, F. Mueller, D. Bresser, I. Lieberwirth, W. Tremel, S. Passerini, R. Zentel, *Macromol. Rapid Commun.* **2015**, *36*, 1075.
[45] W. Kaim, B. Schewerski, *Bioinorganic Chemistry: Inorganic Elements in the Chemistry of Life: An Introduction and Guide (Inorganic Chemistry)*, 1st ed., Wiley, Chichester, UK **1994**.
[46] W. Eck, A. Goelzhaeuser, M. Zharnikov, V. Stadler, W. Geyer, M. Grunze, D. Az(Univ Heidelberg), DE19945935 A1, **2001**.
[47] W. R. McNamara, R. C. SnoebergerIII, G. Li, C. Richter, L. J. Allen, R. L. Milot, C. A. Schmuttenmaer, R. H. Crabtree, G. W. Brudvig, V. S. Batista, *Energy Environ. Sci.* **2009**, *2*, 1173.
[48] A. Klegeris, L. G. Korkina, S. A. Greenfield, *Free Radical Biol. Med.* **1995**, *18*, 215.
[49] T. Rajh, L. X. Chen, K. Lukas, T. Liu, M. C. Thurnauer, D. M. Tiede, *J. Phys. Chem. B* **2002**, *106*, 10543.
[50] M. Niederberger, M. H. Bartl, G. D. Stucky, *Chem. Mater.* **2002**, *14*, 4364.
[51] M. Niederberger, G. Garnweitner, F. Krumeich, R. Nesper, H. Cölfen, M. Antonietti, *Chem. Mater.* **2004**, *16*, 1202.
[52] M. N. Tahir, M. Eberhardt, P. Theato, S. Faiß, A. Janshoff, T. Gorelik, U. Kolb, W. Tremel, *Angew. Chem. Int. Ed.* **2006**, *45*, 908.
[53] M. Yan, F. Chen, J. Zhang, *Chem. Lett.* **2004**, *33*, 1352.
[54] M. Niederberger, M. H. Bartl, G. D. Stucky, *J. Am. Chem. Soc.* **2002**, *124*, 13642.
[55] I. Olliges-Stadler, M. D. Rossell, M. J. Süess, B. Ludi, O. Bunk, J. S. Pedersen, H. Birkedal, M. Niederberger, *Nanoscale* **2013**, *5*, 8517.
[56] D. Su, S. Dou, G. Wang, *Chem. Mater.* **2015**, *27*, 6022.
[57] Z. Hong, K. Zhou, Z. Huang, M. Wei, *Sci. Rep.* **2015**, *5*, 11960.
[58] A. Coelho, *TOPAS-Academic Version 4.1*, Computer Software, Brisbane, Australia **2007**.
[59] R. W. Cheary, A. Coelho, *J. Appl. Crystallogr.* **1992**, *25*, 109.
[60] M. Wagemaker, W. J. H. Borghols, F. M. Mulder, *J. Am. Chem. Soc.* **2007**, *129*, 4323.
[61] D. Shanmukaraj, S. Grugeon, S. Laruelle, G. Douglade, J.-M. Tarascon, M. Armand, *Electrochem. Commun.* **2010**, *12*, 1344.
[62] G. Singh, B. Acebedo, M. C. Cabanas, D. Shanmukaraj, M. Armand, T. Rojo, *Electrochem. Commun.* **2013**, *37*, 61.
[63] D. E. Bergbreiter, P. L. Osburn, C. Li, *Org. Lett.* **2002**, *4*, 737.
[64] D. V. Bavykin, V. N. Parmon, A. A. Lapkin, F. C. Walsh, *J. Mater. Chem.* **2004**, *14*, 3370.

